



Probing the functionality of *nanosstructured* MnCeO_x catalysts in the carbon monoxide oxidation

Part II. Reaction mechanism and kinetic modelling

Francesco Arena^{a,b,*}, Roberto Di Chio^a, Layla Filiciotto^{a,1}, Giuseppe Trunfio^a,
Claudia Espro^a, Alessandra Palella^b, Antonio Patti^c, Lorenzo Spadaro^b

^a Dipartimento di Ingegneria, Università degli Studi di Messina, Viale F. Stagno D'Alcontres 31, I-98166 Messina, Italy

^b Istituto CNR-ITAE "Nicola Giordano", Via Salita S. Lucia 5, I-98126 S. Lucia (Messina), Italy

^c School of Chemistry and ARC Centre of Excellence for Electromaterials Science (ACES), Monash University, Victoria, 3800, Australia



ARTICLE INFO

Article history:

Received 17 May 2017

Received in revised form 3 July 2017

Accepted 8 July 2017

Available online 11 July 2017

Keywords:

Nanosstructured MnCeO_x catalyst

CO oxidation

Reaction mechanism

Kinetic modelling

Active sites and oxygen species

ABSTRACT

The kinetics of the CO oxidation on a typical *nanocomposite* MnCeO_x catalyst (M5C1) were probed by temperature programmed catalytic reaction (TPCR) tests in the range of 293–533 K, varying reagent partial pressure (*i.e.*, p_{CO} and p_{O_2}) between 0.00625 and 0.025 atm (P, 1 atm) (Arena et al., 2017). Experimental data indicate kinetic orders of 0.6 and 0.4 on p_{CO} and p_{O_2} respectively, with apparent activation energy of 40 ± 3 kJ/mol (Arena et al., 2017). A systematic study of the interaction pattern of catalyst with reagent and product molecules shows easy reactivity of surface oxygen to CO, low mobility of lattice oxygen and weak surface affinity to CO₂. Systematic evidences on reaction mechanism and surface intermediates signal an *extrafacial* redox path, triggered by abstraction of oxygen atoms in the neighbouring of active Mn^{IV} sites (Arena et al., 2017), and sustained by O₂ species adsorbed on those surface oxygen vacancies. A Langmuir-Hinshelwood (L-H) reaction mechanism leads to a formal kinetic model explaining the CO oxidation functionality of bare and promoted MnO_x catalysts.

© 2017 Elsevier B.V. All rights reserved.

1. Introduction

Despite a huge research interest focused during last decades on low-cost transition metal oxide (TMO) catalysts, nowadays many environmental catalytic technologies rely on the total oxidation functionality of supported noble-metals, driving the combustion of pollutants in gas and liquid exhausts [2–5]. Among countless model compounds useful to assess the efficiency of new catalyst formulations, carbon monoxide is matter of practical and scientific concerns as it is a highly toxic species for living beings and a precursor of tropospheric ozone, being also a poison for important catalytic technologies (*e.g.*, Ammonia, Fuel Cells, *etc.*). Furthermore, its oxidation is one of the simplest model reactions, commonly employed

in surface science and catalytic studies, to probe the functionality of metal and TMO catalysts [1,2,5].

Beside to the well-known reactivity of supported noble-metals, cobalt-based catalysts are active even at sub-ambient conditions but suffering from relevant deactivation phenomena [5–7], while bare and promoted MnO_x materials exhibit a good CO oxidation performance in low-medium temperature windows (293–573 K) [1,3,5,8–27]. In particular, composite MnCeO_x systems represent a viable alternative to noble-metals for the mineralization of pollutants in gas and liquid phases, although the synthesis method controls physico-chemical and catalytic properties [3,11,17]. Then, despite remarkable structural effects promote surface exposure, dispersion and reducibility of *nanosstructured* MnCeO_x materials [1,3,8,11,17,20–22,27], larger availability of surface active Mn^{IV} sites explains the higher reactivity of the bare MnO_x system in the CO oxidation [1], and the selective aerobic oxidation of benzyl alcohol [27].

It is recognised that conventional supported noble-metals drive a Langmuir-Hinshelwood (L-H) reaction path, accounting for the inhibitory effect of CO and the higher reactivity (*i.e.*, TOF) of large metal particles, while in combination with ceria carrier a dual-site mechanism prevails [5]. At variance, under high O₂ pressure

* Corresponding author at: Dipartimento di Ingegneria, Università degli Studi di Messina, Italy.

E-mail address: Francesco.Arena@unime.it (F. Arena).

¹ Current affiliation: Departamento de Química Organica, Universidad de Córdoba, Campus de Rabanales, Edificio Marie Curie (C-3), Ctra Nnal IV-A, km 396, Córdoba, Spain.

conditions platinum catalysts form a surface oxide layer enabling the stepwise Mars van Krevelen (MvK) redox path [28]. On the other hand, the mechanism for CO oxidation on TMO catalysts is still undefined [2,5,9,11–18,21–24,29], and attempts of kinetic modelling are, thus, fairly sporadic [30,31]. Mechanistic clues are consistent with a L-H path also for bare and promoted MnO_x catalysts [11–18,22–24], while empiric correlations between catalyst reducibility and activity could argue the MvK route [5,16,21,31]. In fact, recent computational studies on model Mn-doped ceria systems predict an easy reactivity of surface Mn–O–Ce bonds and the consequent formation of oxygen vacancies generating, in turn, very reactive diatomic specie (e.g., O_2^- , $\text{O}_2=\text{O}_2^-$, $\text{O}_2=$) under reaction conditions [23,24]. Moreover, IR spectroscopy provides evidence of various intermediates formed by CO at the surface of bare and promoted MnO_x catalysts, even at low temperature and in absence of O_2 [15,21,22,26].

Therefore, after documenting the effects of Ce addition on physico-chemical properties and CO oxidation activity of nanostructured MnCeO_x systems, along with an unchanging reaction mechanism driven by surface Mn^{IV} active sites in the range of 293–533 K, this work addresses kinetic and mechanistic issues of the CO oxidation on a typical nanostructured MnCeO_x catalyst (i.e., M5C1) [1]. Kinetic data in the range of 293–403 K and systematic evidences on the interaction pattern of the catalyst with reagent and product molecules are synthesised into a L-H mechanism and a formal kinetic model predicting the CO oxidation functionality of bare and promoted MnO_x catalysts.

2. Experimental

2.1. Catalysts preparation

The M5C1 catalyst ($\text{Mn}_{\text{at}}/\text{Ce}_{\text{at}}$, 5) was synthesized via the previously described redox-precipitation method [1,27], consisting in the titration of the $\text{Mn}(\text{NO}_3)_2 \cdot 4\text{H}_2\text{O}$ (>97%, Carlo Erba) precursor by an aqueous solution (0.15 L) of KMnO_4 ($\geq 99\%$, Carlo Erba) and $\text{Ce}(\text{NH}_3)_2(\text{NO}_3)_6$ (>98.5%, Aldrich) precursors, at constant pH (4.5 ± 0.5) [32,33]. The M5C1 catalyst has surface area, pore volume, and average pore diameter of $160 \text{ m}^2/\text{g}$, $0.55 \text{ cm}^3/\text{g}$ and 30 nm, respectively [1]. Before measurements, the catalyst samples were pretreated *in situ* under a 5% O_2/He flow at 423 K for 1 h.

2.2. Catalyst characterization

Temperature Programmed Reduction (CO-TPR) measurements in the range of 293–773 K were carried out in a conventional apparatus operating in both continuous and pulse mode, using a 5% CO/He carrier flowing ($60 \text{ stp mL min}^{-1}$) in a quartz micro-reactor (i.d., 4 mm) heated at the rate of 12 K/min (w_{cat} , 20 mg) [1].

Temperature Programmed Desorption (TPD) measurements were carried out in the above apparatus, using He as carrier gas ($60 \text{ stp mL min}^{-1}$) and a heating rate of 12 K/min. Pretreated catalyst samples (20 mg) were cooled at r.t. (298 K) and further treated under 5% CO/He, CO/ O_2 /He ($p_{\text{CO}} = p_{\text{O}_2}$, 0.025 atm) or 10% CO_2 /He flow for 1 h. Thereafter, the catalyst was flushed by the carrier gas and, after baseline stabilization, the (m/z) signals of He (4), H_2O (18), CO (28), O_2 (32) and CO_2 (44) were recorded by a QMS (Hidden Analytical, HPR 20), operating in MID mode with the SEM amplifier at 1200 V [1].

Steady-state O_2 uptake measurements were performed in pulse mode after catalyst (20 mg) exposure to the He/CO/ O_2 reaction mixture (CO/ O_2 , 0.25–3.3) at 393 K for 1 h. After flushing by the He carrier ($35 \text{ stp mL min}^{-1}$), O_2 micro-pulses ($2.7 \cdot 10^{-9} \text{ mol O}_2$) were injected, with no consumption being recorded irrespective of the reaction mixture composition (*v. infra*).

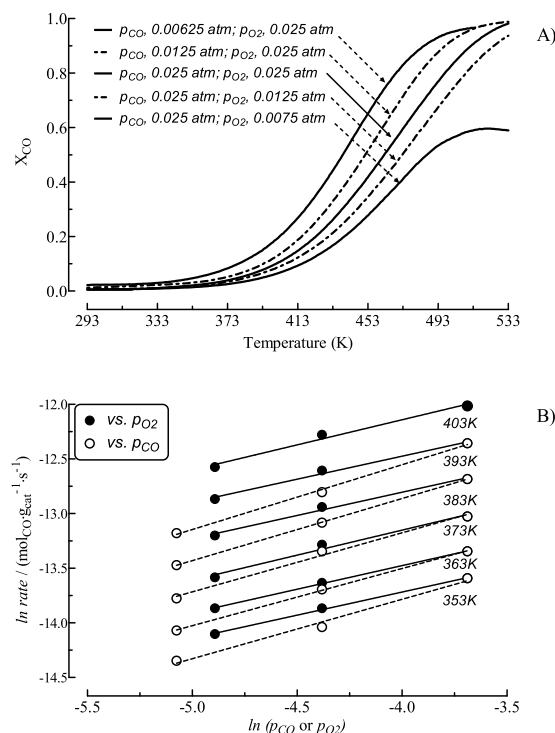


Fig. 1. (A) CO conversion of the M5C1 catalyst in the range of 293–533 K at different p_{CO} and p_{O_2} (F , 60 stp mL/min; P , 1 atm; w_{cat} , 0.02 g); (B) log-plot of rate data in the range of 353–403 K ($X_{\text{CO}} < 12\%$).

2.3. Catalyst testing

CO oxidation kinetic data in the range of 293–533 K were obtained by temperature programmed catalytic reaction (TPCR) tests, feeding a CO/ O_2 /He mixture at the rate of $60 \text{ stp mL min}^{-1}$ (P , 1 atm), with p_{CO} and p_{O_2} varying between 0.00625 and 0.025 atm (w_{cat} , 20 mg). The reaction stream was analysed *on line* by the QMS [1].

Pulse CO oxidation tests were carried out at 393 K injecting five consecutive CO pulses ($1.3 \mu\text{mol}_{\text{CO}}$) on the catalyst (20 mg) kept under 5% O_2/He carrier (35 stp mL/min) and, then, other five pulses under He flow. The CO and CO_2 signals were acquired by the QMS, as above described.

3. Results and discussion

3.1. Reaction kinetics and mechanistic evidences

3.1.1. Empiric kinetics

The kinetics of the CO oxidation on the M5C1 catalyst were probed varying the CO and O_2 pressure in the range of 0.00625–0.025 atm, to ensure “ideal” kinetic conditions and the absence of mass-transfer resistances in the whole conversion range [1]. Activity data at different p_{CO} and p_{O_2} in Fig. 1A show a regular growth of CO conversion to final values comprised between 60 and 100% (533 K), the former depending on the limiting O_2 pressure at the highest $p_{\text{CO}}/p_{\text{O}_2}$ ratio (3.3). Moreover, conversion levels lowering with p_{CO} and rising with p_{O_2} denote a kinetic dependence in-between 0 and 1 for both reagents, as confirmed by the log-plot of rate data in the range of 353–403 K ($X_{\text{CO}} < 12\%$), indicating constant reaction orders of 0.6 and 0.4 with respect to p_{CO} and p_{O_2} , respectively (Fig. 1B). Diagnostic of similar resistances for the activation of CO and O_2 molecules, such a kinetic dependence matches previous literature data for the CO oxidation on composite MnCeO_x [11] and MnO_x catalysts [12–14].

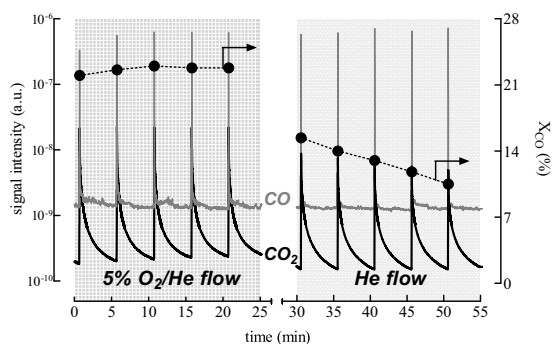


Fig. 2. CO-pulse ($1.3 \mu\text{mol}_{\text{CO}}$) reaction test at 393 K under 5% O_2/He and He carrier flow (F , 35 stp mL/min; w_{cat} , 20 mg).

Isothermal CO pulse oxidation tests (T , 393 K) in presence (5% O_2/He) and absence (He) of oxygen were also carried out to assess the role of the catalyst oxygen on the reactivity pattern [2]. In particular, Fig. 2 shows a constant CO_2 production during five pulses under O_2/He carrier flow, corresponding to a steady CO conversion of 22–23%, whereas under He flow the conversion attains an initial value of 15%, lowering progressively in the successive four pulses. Considering that each CO pulse corresponds to only 0.1% of reactive catalyst oxygen ($6.3 \cdot 10^{-3} \text{ mol O}_2/\text{g}_{\text{cat}}$) [1,27], this signals a negligible, if any, role of lattice oxygen on the reactivity of the M5C1 catalyst. In fact, the lack of O_2 uptake at the steady state discloses a fully oxidized status of the catalyst that rules out the typical stepwise MnV redox path since, for comparable resistances of the reduction and oxidation steps, it predicts a significant catalyst reduction at steady-state conditions [2].

3.1.2. Reactivity and mobility of catalyst oxygen

Reactivity and mobility of oxygen species are very crucial issues for the functionality of TMO oxidation catalysts [2,5], here probed by temperature programmed analyses. In particular, the reactivity of catalyst oxygen toward the substrate was assessed by CO-TPR analysis (Fig. 3A), while the O_2 -TPD profiles of the catalyst treated under CO, CO/O_2 or CO_2 flow (298 K) provide basic information on the mobility of lattice oxygen species (Fig. 3B). The CO-TPR pattern documents an easy reduction of the MnO_x phase at 293 K, previ-

ously ascribed to the high reactivity of surface Mn^{IV} sites toward CO [1,27], while a poor mobility of lattice oxygen ions under reaction conditions is evident from the O_2 -TPD pattern. Indeed, irrespective of treatment atmosphere, these show an analogous O_2 desorption band in the range of 593–973 K, with an inflexion point at 743 K and two maxima at 753 and 913 K, accounting for thermal reduction of surface and bulk MnO_x species. In particular, the former is attributable to a maximum O_2 desorption rate from surface MnO_2 sites, while the two sharp maxima arise from the stepwise decomposition of sub-surface and bulk MnO_x phases to Mn_3O_4 , according to an overall release of $2.0 \pm 0.1 \text{ mmol O}_2/\text{g}_{\text{cat}}$ [29]. Additionally, the catalyst samples treated under CO/O_2 and CO_2 streams also feature a small O_2 peak in the range of 293–493 K, ascribable to adsorbed (diatomic) oxygen species (Fig. 3B) [11,22,33]. Its absence in the profile of the sample treated under CO proves the high reactivity of such oxygen species, forming CO_2 already at 298 K (Fig. 3A), while a higher intensity for the sample exposed to the CO/O_2 reaction mixture indicates an over-oxidized status of the catalyst, explaining the lack of oxygen uptake at steady-state (*v. supra*).

3.1.3. Surface interactions and reaction intermediates

A summary of IR spectroscopy data, useful to shed light into the surface interactions of CO with MnO_x and MnCeO_x systems in the range of 85–673 K, both in absence and presence of O_2 , is presented in Table 2 [15,21,22,26]. Beside to signals in the ranges of $2100\text{--}2200 \text{ cm}^{-1}$ and $2300\text{--}2400 \text{ cm}^{-1}$, typical of gas phase or weakly interacting CO, and free carbonate species respectively, Table 2 shows consensus on bands at $1217\text{--}1233$, $1340\text{--}1381$ ($1455\text{--}1470$), and $1552\text{--}1580 \text{ cm}^{-1}$, reasonably ascribable to bridged, unidentate and bidentate carbonate intermediates, respectively (Scheme 1 of SI) [34]. Their occurrence in both presence and absence of O_2 , even at 85 K [15], supports the high reactivity of surface oxygen species toward CO, although it can be noticed that the signal of the bidentate species (1565 cm^{-1}) generally occurs at low temperature ($\leq 298 \text{ K}$) in presence of O_2 and at $T \geq 393 \text{ K}$ in its absence (Table 2). Then, further insights into genesis and stability of these intermediates are attained from the CO_x TPD profiles of catalyst samples exposed to CO, CO/O_2 and CO_2 atmosphere (298 K), shown in Fig. 4. The lack of any CO signal and similar CO_2 profiles in the range of 293–643 K prove a strong interaction of

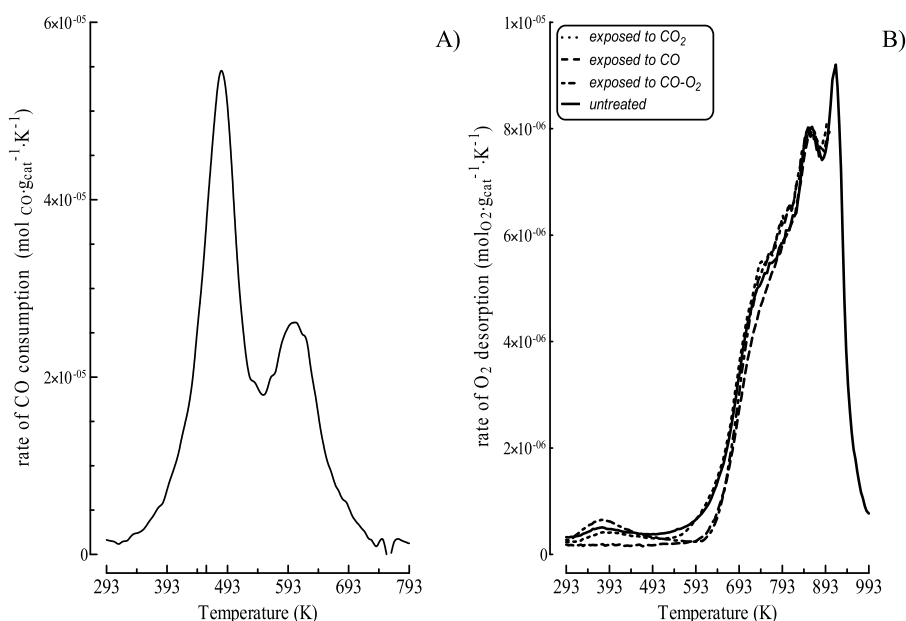


Fig. 3. (A) CO-TPR profile of the M5C1 catalyst; (B) O_2 -TPD pattern of the M5C1 catalyst exposed to CO, CO/O_2 and CO_2 flow at 298 K (1 h).

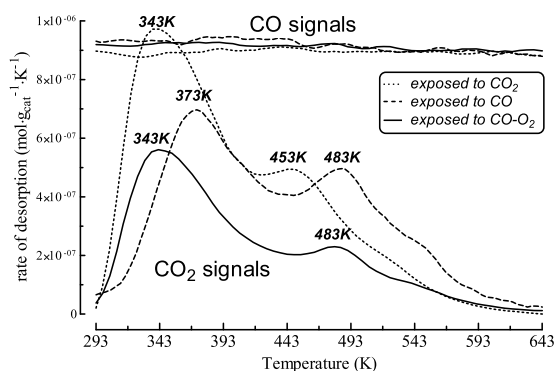


Fig. 4. TPD profiles of CO and CO₂ of the M5C1 catalyst exposed to CO, CO/O₂ and CO₂ flow at 298 K (1 h).

CO at the catalyst surface, leading to an easy formation of CO₂ also in absence of O₂. In particular, the sample exposed to CO₂ shows a main peak centred at 343 K and a secondary maximum at 443 K, accounting for an uptake (250 μmol/g) in agreement with previous estimates of basic sites on similar catalysts [35]. The sample treated in CO shows a CO₂ profile characterised by a main peak centred at 373 K, with another incipient maximum at 483 K, the intensity of which corresponds to 70% of previous one (170 μmol/g). At least, the sample exposed to the CO/O₂ mixture shows the smallest CO₂ release (110 μmol/g), likely consequence of a lower stability of surface intermediates in presence of O₂ [15,21], which still consists of a main peak at 343 K with another poorly resolved maximum at 483 K. Overall, low desorption temperature, small uptake and desorption rate minor by two orders of magnitude than the rate of CO₂ formation by reduction (Fig. 3A) substantiate a weak interaction of CO₂ with the M5C1 catalyst surface [23].

The qualitative features of the CO₂ TPD profiles are also related to the above intermediates, arising from the surface interactions of CO in presence and absence of O₂. In particular, the *bidentate* species occurs mostly in presence of O₂ and, according to the 30 K downward shift of the main desorption peak (Fig. 4), it is less stable than the *bridged* intermediate formed by the interaction of CO with catalyst surface oxygen. While, the small peak at high temperature is likely due to the most stable *unidentate* species, resulting from the interaction of CO₂ with a typical surface basic site (Scheme 1) [15,23,26,34]. At least, the similar CO₂ TPD pattern after exposure under CO-O₂ and CO₂ atmosphere discloses a reversible formation of the *bidentate* and *unidentate* intermediates [34], explaining the negative effect of CO₂ co-feeding on the CO oxidation performance of the M5C1 catalyst [18].

3.2. Reaction mechanism and kinetic modelling

3.2.1. Reaction mechanism

Despite the large number of studies devoted during last decades at ascertaining the CO oxidation functionality of MnO_x catalysts, reaction mechanism, active sites and nature of oxygen species are still matter of debate. In fact, type of oxide phase, nature of supports and promoters, and a crucial influence of the reaction atmosphere on the surface structure shape the functionality of MnO_x-based systems [1,9–16,19,29], similarly to noble-metal systems [5,28]. Thus, while strict relationships between catalyst reducibility and activity could reveal a typical MvK redox mechanism, both theoretical and experimental clues support a relevant influence of adsorption phenomena in the studied range of temperature (293–533 K) [12–15,21–24,26,34]. Predicted by quantum-chemical data on model Mn^{IV}/CeO₂ systems [23,24], in fact, electrophilic character of oxygen atoms of the MnO_x phase (e.g., O₁) [1], and electron-donor

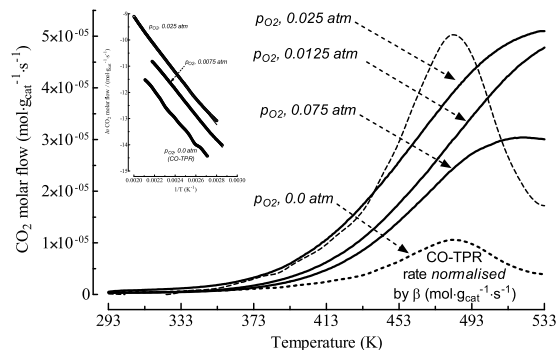


Fig. 5. Rate of CO₂ formation at various p_{O_2} (0.0–0.025 atm) and relative Arrhenius plot of CO₂ rate in the range of 373–473 K (inset).

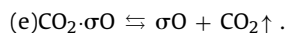
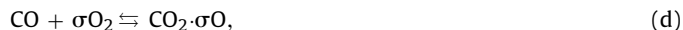
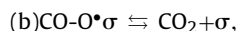
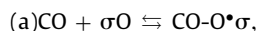
behaviour of the CO molecule [22] explain the interaction pattern of CO at the surface of MnO_x catalyst.

Moreover, analogous trends of the CO₂ rate in CO-TPR and TPCR tests (Fig. 5) indicate an unchanging activation energy (40–42 kJ/mol), signalling that the formation of surface oxygen vacancies is the *rate determining step* (r.d.s.) of the catalytic reaction cycle [1,11–18,21–25]. According to previous evidences on the same activation energy (41 ± 3 kJ/mol) for (M1C1-R4) catalyst reduction and CO oxidation [11], such values also match the energetic barrier (0.22–0.37 eV) for the formation of surface oxygen vacancies by CO on the model Mn_{0.125}Ce_{0.875}O₂ system [23].

Furthermore, the reaction mechanism must explain all the following experimental findings:

- a similar fractional kinetic dependence on p_{CO} and p_{O_2} (Fig. 1);
- a strong surface interaction of CO, leading to the above surface intermediates (Fig. 4);
- an “easy” abstraction of oxygen atoms from surface Mn^{IV} sites (Fig. 3A);
- a significant kinetic effect of gas phase O₂ on activity (Fig. 2);
- a poor mobility of lattice oxygen ions under reaction condition (Fig. 3B);
- a poor catalyst affinity to CO₂, also weakening in presence of O₂ (Fig. 4).

In fact, all these evidences are consistent with an *extrafacial* L-H reaction path [2,11,21–24,29]



In particular, it consists of the following five elementary steps:

- the adsorption of CO on the active Mn^{IV} sites (σO), leading to the $\sigma O \cdot CO$ intermediate;
- the decomposition of the latter into a CO₂ molecule and a surface oxygen vacancy (σ);
- the adsorption of O₂ on σ , forming the reactive diatomic oxygen species (σO_2);
- the interaction of a second CO molecule with σO_2 , yielding the $\sigma O \cdot CO_2$ intermediate;
- the decomposition of the latter into CO₂, with replenishment of the active site (σO).

Table 1Influence of CO and O₂ partial pressure on reaction rate at various temperatures (Fig. 1A).

reagent pressure (atm)		Temperature (K)					
<i>p</i> _{O2}	<i>p</i> _{CO}	353	363	373	383	393	403
		reaction rate (mol _{CO} g _{cat} ⁻¹ s ⁻¹)					
0.0075	0.025	7.5·10 ⁻⁷	9.5·10 ⁻⁷	1.3·10 ⁻⁶	1.9·10 ⁻⁶	2.6·10 ⁻⁶	3.5·10 ⁻⁶
0.0125	0.025	9.5·10 ⁻⁷	1.2·10 ⁻⁶	1.7·10 ⁻⁶	2.4·10 ⁻⁶	3.4·10 ⁻⁶	4.7·10 ⁻⁶
0.025	0.025	1.3·10 ⁻⁶	1.6·10 ⁻⁶	2.2·10 ⁻⁶	3.1·10 ⁻⁶	4.3·10 ⁻⁶	6.1·10 ⁻⁶
0.025	0.00625	5.9·10 ⁻⁷	7.8·10 ⁻⁷	1.0·10 ⁻⁶	1.4·10 ⁻⁶	1.9·10 ⁻⁶	n.d.
0.025	0.0125	8.5·10 ⁻⁷	1.1·10 ⁻⁶	1.6·10 ⁻⁶	2.1·10 ⁻⁶	2.8·10 ⁻⁶	n.d.
0.025	0.025	1.3·10 ⁻⁶	1.6·10 ⁻⁶	2.2·10 ⁻⁶	3.1·10 ⁻⁶	4.3·10 ⁻⁶	6.1·10 ⁻⁶

Table 2Summary of literature IR spectroscopy data for CO adsorption on MnO_x and MnCeO_x materials.

Sample	Exp. Conditions	IR signals (cm ⁻¹)						Ref.
MnCeO _x	CO/O ₂ ; T, 298–393 K	2113–2173						[22]
		2340–2360		1568	1470	1390	1217	
MnCeO _x	CO; T, 298 K	2330		1614	1533	1348	1218	[21]
	CO; T, 673 K	2400–2300			1568	1533	1394	
	CO/O ₂ ; T, 298 K			1609	1565	1395	1218	
	CO/O ₂ ; T, 673 K				1565	1526	1348	
MnO _x	CO; T, 298 K			1675		1340	1220	[15]
	CO; T, 673 K	2360	2113–2150			1494,1418	1360	
	CO/O ₂ ; T, 298 K		2117–2173	1670	1568	1340	1220	
	CO/O ₂ ; T, 673 K	2300–2400	2117–2173		1580	1525	1359–1381	
MnO _x /YSZ	CO; T, 85 K	2161		1657		1375		[15]
	CO; T, 298 K			1605		1455	1333	
MnO _x /Al ₂ O ₃	CO; T, 100 K		2170–2180				1224	[26]
MnCeO _x /Al ₂ O ₃	CO; T, 473–673 K			1768	1552	1456	1384	

This accounts for all above literature and experimental evidences explaining, in particular, a general correlation between activity and catalyst reducibility, although the remarkable kinetic effect of *p*_{O2} (Fig. 1) proves that gas phase O₂ actually sustains the overall catalytic cycle. Noteworthy, it also elucidates the interactions leading to the different intermediates. Indeed, the σO·CO₂ species matches structure and stoichiometry of the *bidentate* carbonate, which is generated by interaction of CO with diatomic oxygen species adsorbed on the surface oxygen vacancies (e.g., O₂–, O₂=O₂–; O₂=) [22–24,34], while the σO·CO intermediate mirrors the basic features of the *bridged* carbonate, arising from the interaction of CO with two oxidized active Mn^{IV} sites (σO) [15,23,26,34]. The latter leads to the formation of CO₂ and a reduced active site (σ) via a “2-electron” transfer process to the Mn^{IV} site (step 2), at variance with *bidentate* species benefitting from the enhanced electrophilic character of adsorbed diatomic oxygen species to drive the CO oxidation (step 4). Finally, mechanistic clues suggest the role of *spectator* species for the *unidentate* intermediate [15,21–23,26,34].

3.2.2. Kinetic modelling

Despite the small number of elementary steps, some conventional approximations are necessary to get a friendly form of the kinetic equation from the above reaction mechanism. Namely, supported by the fact that the same intermediates occur under CO and CO₂ atmosphere (Fig. 4) [34], the CO adsorption (a) and CO₂ desorption steps (e) are assumed at equilibrium (*q.e.*) and, using the approximation of *irreversible step* (*i.s.*) for b (*r.d.s.*), c (*fast*), and d (*fast*) ones, the following thermodynamic and kinetic relationships can be written

$$K_1 = \frac{[\sigma\text{O} \cdot \text{CO}]}{p_{\text{CO}} \cdot [\sigma\text{O}]} \quad \text{q.e. (1),}$$

$$r_2 = k_2 \cdot [\sigma\text{OCO}] \quad \text{i.s. (2),}$$

$$r_3 = k_3 \cdot p_{\text{O}_2} \cdot [\sigma] \quad \text{i.s. (3),}$$

$$r_4 = k_4 \cdot p_{\text{CO}} \cdot [\sigma\text{O}_2] \quad \text{i.s. (4),}$$

$$K_5 = \frac{[\sigma\text{O}] \cdot p_{\text{CO}_2}}{[\sigma\text{O} \cdot \text{CO}_2]} \quad \text{q.e. (5),}$$

The assumption of *steady-state* further involves the same rate for steps b–d (*rate* = *r*₂ = *r*₃ = *r*₄), leading to the following expression for the mass balance of surface sites and intermediates

$$1 = [\sigma\text{O}] \cdot \left[1 + K_1 \cdot p_{\text{CO}} + \frac{K_1 \cdot k_2 \cdot p_{\text{CO}}}{k_3 \cdot p_{\text{O}_2}} + \frac{K_1 \cdot k_2}{k_4} + \frac{p_{\text{CO}_2}}{K_5} \right] \quad (6)$$

Neglecting the last term in view of the weak interaction of CO₂ with catalyst surface [15,21–24,34], and very small *p*_{CO2} (<2.5·10⁻³ atm) for differential CO conversion, the expression for the fraction of oxidized active sites (*i.e.*, in the fundamental status)

$$[\sigma\text{O}] = \frac{1}{1 + K_1 \cdot p_{\text{CO}} + \frac{K_1 \cdot k_2 \cdot p_{\text{CO}}}{k_3 \cdot p_{\text{O}_2}} + \frac{K_1 \cdot k_2}{k_4}} \quad (7),$$

leads to the final equation rate

$$\text{rate} = \frac{K_1 \cdot k_2 \cdot k_3 \cdot k_4 \cdot p_{\text{CO}} \cdot p_{\text{O}_2}}{k_3 \cdot k_4 \cdot p_{\text{O}_2} + K_1 \cdot k_3 \cdot k_4 \cdot p_{\text{CO}} \cdot p_{\text{O}_2} + K_1 \cdot k_2 \cdot k_4 \cdot p_{\text{CO}} + K_1 \cdot k_2 \cdot k_3 \cdot p_{\text{O}_2}} \quad (8).$$

Hence, the Eq. (8) was transformed into the sum of the various kinetic resistances

$$\frac{p_{\text{CO}} \cdot p_{\text{O}_2}}{\text{rate}} = \frac{p_{\text{O}_2}}{(K_1 \cdot k_2)} + \frac{p_{\text{O}_2}}{k_4} + \frac{p_{\text{CO}} \cdot p_{\text{O}_2}}{k_2} + \frac{p_{\text{CO}}}{k_3} \quad (9),$$

to evaluate the main kinetic parameters and ascertain consistency and reliability of the reaction mechanism. Rate data (Table 1) elaborated by Eq. (9), in fact, provide two series of straight-line relationships as function of both *p*_{CO} (Fig. 6A) and *p*_{O2} (Fig. 6B), slope and intercept values of which provide the kinetic constants *k*₂, *k*₃ and *k*_{CO2} in the range of 353–403 K (see App. A of SI), listed in Table 3. In particular, mathematical relationships show that the latter corresponds to the cumulative constant of CO₂ formation, including the (*K*₁·*k*₂) and *k*₄ terms (App. A of SI). Referring to the reaction step of

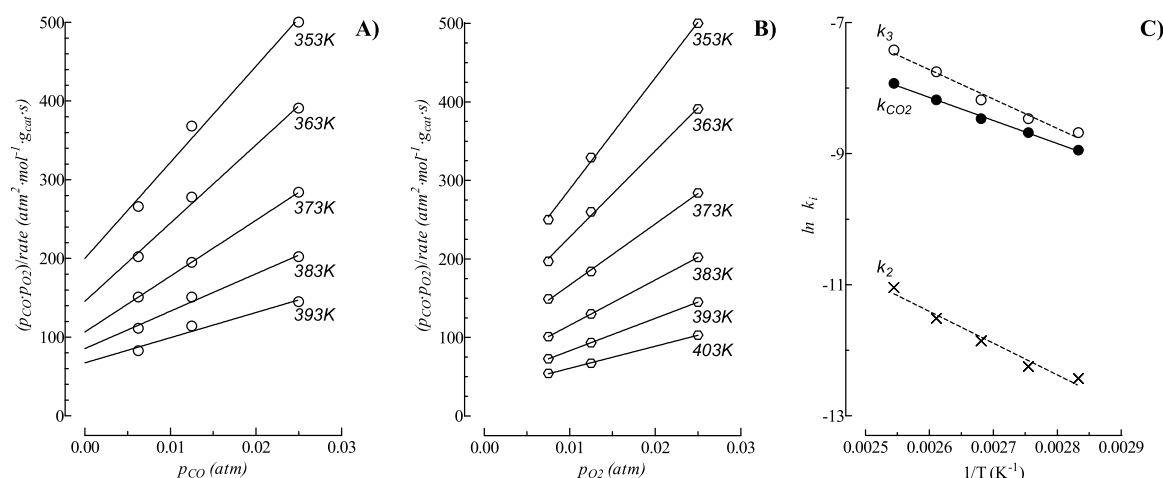


Fig. 6. Elaboration of rate data by Eq. (9) as a function of p_{CO} (A) and p_{O_2} (B) and Arrhenius plot of the kinetic constants k_2 , k_3 and k_{CO_2} (C).

Table 3

Slope and intercept values of the straight-line relationships obtained from rate data elaborated by the eq. 9 (Fig. 6), and kinetic constant values of the various reaction steps (see App. A of SI).

T (K)	slope _{CO}	intercept _{CO}	slope _{O2}	intercept _{O2}	k_2 (mol g _{cat} ⁻¹ s ⁻¹)	k_3 (mol g _{cat} ⁻¹ s ⁻¹ atm _{O2} ⁻¹)	k_{CO_2} (mol g _{cat} ⁻¹ s ⁻¹ atm _{CO} ⁻¹)
353	12,210 ± 1426	200 ± 24	14,170 ± 471	147 ± 8	4.0·10 ⁻⁶	1.7·10 ⁻⁴	1.3·10 ⁻⁴
363	9931 ± 772	146 ± 13	10,970 ± 471	118 ± 1	4.8·10 ⁻⁶	2.1·10 ⁻⁴	1.7·10 ⁻⁴
373	7097 ± 20	107 ± 1	8757 ± 396	89 ± 4	7.1·10 ⁻⁶	2.8·10 ⁻⁴	2.1·10 ⁻⁴
383	4743 ± 574	86 ± 10	6194 ± 376	58 ± 1	1.0·10 ⁻⁵	4.3·10 ⁻⁴	2.8·10 ⁻⁴
393	3198 ± 622	67 ± 10	4445 ± 267	42 ± 1	1.6·10 ⁻⁵	6.0·10 ⁻⁴	3.6·10 ⁻⁴
403	n.d.	n.d.	3051 ± 162	33 ± 1	n.d.	7.6·10 ⁻⁴	n.d.

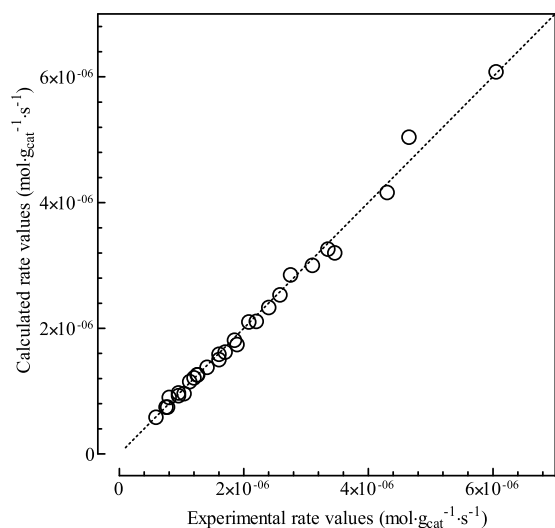


Fig. 7. Calculated vs. experimental rate values in the range of 353–403 K at different p_{CO} and p_{O_2} (see Table 1).

the $\sigma O\cdots CO$ intermediate, the constant k_2 (mol g_{cat}⁻¹ s⁻¹) is insensitive to the reagent pressure resulting, thus, systematically smaller than k_{CO_2} and k_3 (mol g_{cat}⁻¹ s⁻¹ atm⁻¹) by almost two orders of magnitude (Table 3). However, an analogous temperature dependence (Fig. 6C) indicates that the energetic barrier of 40 ± 3 kJ/mol is due to reduction of surface-active Mn^{IV} sites (Fig. 5) driving, in turn, the non-activated reaction cycle involving gas phase O₂ [22–24]. Thus, matching theoretical and experimental evidences, the proposed reaction mechanism and its kinetic model provide a definitive account of the CO oxidation functionality of the MnCeO_x system, confirmed by the agreement of calculated rate values with experimental rate data (Table 1), observable in Fig. 7.

3.2.3. Active sites and TOF

The last issue of the CO oxidation functionality of the M5C1 catalyst remains the population of active sites that, according to mechanistic findings, should be the most reactive surface Mn^{IV} centres. This supports the idea that the rising branch of the main CO-TPR peak monitors the reduction of surface active Mn^{IV} sites (σO) [1,11,27,33]. Since the ideal kinetic regime of CO-TPR measurements, substantiated by a maximum CO consumption lower than 5% [1,27,36], and reduction kinetics insensitive to the concentration of the surface Mn^{IV} sites (e.g., $rate_{red} = k_{red} \cdot p_{CO} = k'$) [37], their reduction rate depends only on temperature (Fig. 5B). In fact, a constant activation energy (41 kJ/mol) in the range of 373–473 K (Fig. 3A), relative to reduction of surface active sites, explains the unchanged reaction mechanism occurring on MnO_x and MnCeO_x catalysts in the above temperature range [1,11–14]. Thus, a population of surface Mn^{IV} sites of $1.85 \cdot 10^{-3}$ mol/g_{cat}, given by the integral of the CO-TPR curve between 293 and 473 K (Fig. 3A), accounts for a remarkable 30% MnO_x dispersion and, in turn, for TOF values in the order of 10^{-3} – 10^{-1} s⁻¹, comparing to those of noble-metal catalysts under similar reaction conditions [5].

4. Conclusions

Mechanistic and kinetic issues of CO oxidation on a nanostructured MnCeO_x catalyst are summarised in the following conclusions:

- low lattice oxygen mobility and significant kinetic effect of p_{O_2} rule out a typical step-wise MvK redox mechanism;
- high reactivity of surface oxygen to CO signals an extrafacial redox path, triggered by abstraction of oxygen atoms in the neighbouring of active Mn^{IV} sites, and sustained by O₂ species adsorbed on those surface oxygen vacancies;
- adsorption of reagent and product molecules leads to formation of bidentate, bridged, and unidentate carbonate intermediates;

- the decomposition of the *bridged* intermediate is the r.d.s. of the CO oxidation, while the reactive *bidentate* intermediate occurs under steady-state conditions;
- a Langmuir–Hinshelwood mechanism predicts the reactivity of nanostructured MnO_x catalysts in the CO oxidation.

Appendix A. Supplementary data

Supplementary data associated with this article can be found, in the online version, at <http://dx.doi.org/10.1016/j.apcatb.2017.07.018>.

References

- [1] F. Arena, R. Di Chio, B. Fazio, C. Espro, L. Spiccia, A. Palella, L. Spadaro, Appl. Catal. B: Environ. 210 (2017) 14–22.
- [2] A. Bielański, J. Haber, Oxygen in Catalysis, Marcel, Dekker Inc., New York, 1991.
- [3] F. Arena, Catal. Sci. Technol. 4 (2014) 1890–1898.
- [4] F. Arena, R. Di Chio, B. Gumina, L. Spadaro, G. Trunfio, Inorg. Chim. Acta 431 (2015) 101–109.
- [5] S. Royer, D. Drupez, ChemCatChem 3 (2011) 24–65.
- [6] Y. Yu, T. Takei, H. Ohashi, H. He, X. Zhang, M. Haruta, J. Catal. 267 (2009) 121–128.
- [7] Y. Lou, L. Wang, Z. Zhao, Y. Zhang, Z. Zhang, G. Lu, Y. Guo, Appl. Catal. B: Environ. 146 (2014) 43–49.
- [8] P. Zhang, H. Lu, Y. Zhou, L. Zhang, Z. Wu, S. Yang, H. Shi, Q. Zhu, Y. Chen, S. Dai, Nat. Commun. 6 (2015) 1–10.
- [9] S. Liang, F. Teng, G. Bulgan, R. Zong, Y. Zhu, J. Phys. Chem. C 112 (2008) 5307–5315.
- [10] K. Frey, V. Iablokov, G. Sáfrán, J. Osán, I. Sajó, R. Szukiewicz, S. Chenakin, N. Kruse, J. Catal. 287 (2012) 30–36.
- [11] F. Arena, G. Trunfio, B. Fazio, J. Negro, L. Spadaro, J. Phys. Chem. C 113 (2009) 2822–2829.
- [12] J. Xu, Y.-Q. Deng, Y. Luo, W. Mao, X.-J. Yang, Y.-F. Han, J. Catal. 300 (2013) 225–234.
- [13] J. Xu, Y.-Q. Deng, X.-M. Zhang, Y. Luo, W. Mao, X.-J. Yang, L. Ouyang, P. Tian, Y.-F. Han, ACS Catal. 4 (2014) 4106–4115.
- [14] K. Ramesh, L. Chen, F. Chen, Y. Liu, Z. Whang, Y.-F. Han, Catal. Today 131 (2008) 477–482.
- [15] R. Craciun, B. Nentwick, K. Hadjiivanov, H. Knözinger, Appl. Catal. A: Gen. 243 (2003) 67–79.
- [16] K. Morgan, K.J. Cole, A. Goguet, C. Hardacre, G.J. Hutchings, N. Maguire, S.O. Shekhtman, S.H. Taylor, J. Catal. 276 (2010) 38–48.
- [17] F. Arena, G. Trunfio, J. Negro, C. Saja, A. Raneri, L. Spadaro, Stud. Surf. Sci. Catal. 175 (2010) 493–496.
- [18] J.-H. Park, D.-C. Kang, S.-J. Park, C.-H. Shin, J. Ind. Eng. Chem. 25 (2015) 250–257.
- [19] J. Jia, P. Zhang, L. Chen, Appl. Catal. B: Environ. 189 (2016) 210–218.
- [20] P. Venkataswamy, K.N. Rao, D. Jampaiah, B.M. Reddy, Appl. Catal. B: Environ. 162 (2015) 122–132.
- [21] X.-m. Zhang, Y.-Q. Deng, P. Tian, H.-h. Shang, J. Xu, Y.-F. Han, Appl. Catal. B: Environ. 191 (2016) 179–191.
- [22] Z.-Q. Zou, M. Meng, Y.-Q. Zha, J. Phys. Chem. C 114 (2010) 468–477.
- [23] L.-C. Hsu, M.-K. Tsai, Y.-H. Lu, H.-T. Chen, J. Phys. Chem. C 117 (2013) 433–441.
- [24] W. Cen, Y. Liu, Z. Wu, H. Wang, X. Weng, Phys. Chem. Chem. Phys. 14 (2012) 5769–5777.
- [25] X. Zhang, J. Wei, X. Liu, W. Liu, C. Zhang, Y. Yang, Eur. J. Inorg. Chem. 25 (2013) 4443–4449.
- [26] N. Drenchev, I. Spassova, E. Ivanova, M. Khristova, K. Hadjiivanov, Appl. Catal. B: Environ. 138–139 (2013) 362–372.
- [27] F. Arena, B. Gumina, A.F. Lombardo, C. Espro, A. Patti, L. Spadaro, L. Spiccia, Appl. Catal. B: Environ. 162 (2015) 260–267.
- [28] B.L.M. Hendriksen, J.M.W. Frenken, Phys. Rev. Lett. 89 (4) (2002) 046101.
- [29] M.I. Zaki, M.A. Hasan, L. Pasupulaty, K. Kumari, Thermochim. Acta 311 (1998) 97–103.
- [30] S. Wagloehener, D. Reichert, D. Leon-Sorzano, P. Balle, B. Geiger, S. Kureti, J. Catal. 260 (2008) 305–314.
- [31] J.L. Ayastuy, A. Gurbani, M.P. Gonzales-Marcos, M.A. Gutierrez-Ortiz, Ind. Eng. Chem. Res. 48 (2009) 5633–5641.
- [32] F. Arena, L. Spadaro, WO 2012168957 (A1), 2012.
- [33] F. Arena, G. Trunfio, J. Negro, B. Fazio, L. Spadaro, Chem. Mater. 19 (2007) 2269–2276.
- [34] C. Li, Y. Sakata, T. Arai, K. Domen, K. Maruya, T. Onishi, J. Chem Soc. Faraday Trans. 1 85 (1989) 929–943.
- [35] C. Cannilla, G. Bonura, F. Arena, E. Rombi, F. Frusteri, Catal. Today 195 (2012) 32–43.
- [36] P. Malet, A. Caballero, J. Chem. Soc. Faraday Trans. 1 (84) (1988) 2369–2375.
- [37] K. Piotrowski, K. Mondal, H. Lorethova, L. Stonawski, T. Szymanski, T. Wiltowski, Int. J. Hydrogen Energy 30 (2005) 1543–1554.